



1 **Quality-controlled meteorological datasets from SIGMA**  
2 **automatic weather stations in northwest Greenland, 2012–**  
3 **2020**

4 Motoshi Nishimura<sup>1\*</sup>, Teruo Aoki<sup>1</sup>, Masashi Niwano<sup>2</sup>, Sumito Matoba<sup>3</sup>, Tomonori  
5 Tanikawa<sup>2</sup>, Tetsuhide Yamasaki<sup>4</sup>, Satoru Yamaguchi<sup>5</sup>, Koji Fujita<sup>6</sup>

6 <sup>1</sup>National Institute of Polar Research, Tokyo, Japan

7 <sup>2</sup>Meteorological Research Institute, Japan Meteorological Agency, Ibaraki, Japan

8 <sup>3</sup>Institute of Low Temperature Science, Hokkaido University, Hokkaido, Japan

9 <sup>4</sup>Avangnaq Arctic Project, Osaka, Japan

10 <sup>5</sup>Snow and Ice Research Center, National Research Institute for Earth Science and Disaster Resilience,  
11 Niigata, Japan

12 <sup>6</sup>Graduate School of Environmental Studies, Nagoya University, Nagoya, Japan

13 *Correspondence to:* Motoshi Nishimura (nishimura.motoshi@nipr.ac.jp)

14 **Abstract.** In situ meteorological data are essential to better understand ongoing environmental  
15 changes in the Arctic. Here, we present a dataset of quality-controlled meteorological observations by  
16 two automatic weather stations in northwest Greenland from July 2012 to the end of August 2020.  
17 The stations were installed in an accumulation area on the Greenland Ice Sheet (SIGMA-A site, 1490  
18 m a.s.l.) and near the equilibrium line of the Qaanaaq Ice Cap (SIGMA-B site, 944 m a.s.l.). We  
19 describe the two-step sequence of quality-control procedures that we used to create increasingly  
20 reliable datasets by masking erroneous data records. We analyzed the resulting 2012–2020 time series  
21 of air temperature, positive degree-days, snow height, surface albedo, and histograms of longwave  
22 radiation (a proxy of cloud formation frequency). We found that snow height increased and albedo  
23 remained steady at the SIGMA-A site, whereas high air temperatures and clear-sky conditions  
24 prevailed while snow height and albedo decreased in the summers of 2015, 2019, and 2020 at the  
25 SIGMA-B site. Therefore, it appears that these weather conditions led to notable snow height  
26 degradation at the SIGMA-B site but not at the SIGMA-A site. We anticipate that this quality-control  
27 method and these datasets will aid in climate studies of northwest Greenland as well as contribute to  
28 the advancement of broader polar climate studies.

29 **1. Introduction**

30 Recent changes of the Greenland Ice Sheet have likely contributed to the global rise in sea level



31 (e.g., IPCC, 2021). These changes include rising air temperature on the ice sheet, the increasing extent  
32 of bare and dark ice (Shimada et al., 2016), and the loss of ice mass (Hanna et al., 2013; IMBIE Team,  
33 2020). Many studies have used regional climate models and atmospheric reanalysis data (e.g., Niwano  
34 et al., 2018; Fettweis et al., 2020) to reveal major ablation events in Greenland and to reconstruct the  
35 long-term past surface mass balance of the Greenland Ice Sheet. In situ meteorological data provide  
36 vital information to monitor environmental changes and inform the models that simulate them;  
37 however, the existing in situ meteorological data are insufficient for these purposes.

38 Some automatic weather station (AWS) networks have been constructed on the Greenland Ice  
39 Sheet, including GC-Net (Steffen and Box, 2001) and PROMICE (van As et al., 2011; Fausto et al.,  
40 2021), and have provided important long-term meteorological data. To contribute to these efforts and  
41 to fill a spatial gap, we established two AWS systems in northwest Greenland (Fig. 1), where rapid  
42 environmental changes have occurred in recent years (Aoki et al., 2014). Recent studies of this region  
43 have documented a drastic mass loss since the mid-2000s (Mouginot et al., 2019), an expansion of the  
44 ablation area (Noël et al., 2019), and a hot spot of increasing rainfall (Niwano et al., 2021). The two  
45 sites were established in 2012 as a part of the Snow Impurity and Glacial Microbe effects on abrupt  
46 warming in the Arctic (SIGMA) Project, which aimed to clarify the dramatic enhancement of melting  
47 of the Greenland Ice Sheet induced by snow impurities (e.g., black carbon, mineral dust). The  
48 observational data acquired since that time have been used by glaciological (Yamaguchi et al., 2014;  
49 Tsutaki et al., 2017; Matoba et al., 2018; Kurosaki et al., 2020), meteorological (Aoki et al., 2014;  
50 Tanikawa et al., 2014; Niwano et al., 2015; Hirose et al., 2021), and biological studies (Onuma et al.,  
51 2018; Takeuchi et al., 2018). These data are also valuable because they support the analytical values  
52 of various numerical models (e.g., Niwano et al., 2018; Fujita et al., 2021) and form the basis for  
53 robust analytical results.

54 The datasets from AWS generally contain erroneous data records that are attributed to sensor noise  
55 or natural factors. Various procedures exist for improving the accuracy of such datasets (e.g., Fiebrich  
56 et al., 2010; Fausto et al., 2021). In particular, careful QC procedures are required for downward  
57 radiation sensors, which are sensitive to solar zenith angle, icing, riming, and snowfall (van den Broeke  
58 et al., 2004a, b; Moradi, 2009). Other QC procedures deal with error sources through range, step, and  
59 internal consistency tests (Estévez et al., 2011). The specifics of QC methods, for example, the  
60 threshold value for detecting erroneous data records, should be adjusted for each observation  
61 environment. In this paper, we describe the QC methods used for the in situ meteorological observation  
62 data from northwest Greenland, which include existing QC methods, new ones, and combinations of  
63 both.

64 After describing the AWS sites (Sect. 2) and their datasets (Sect. 3), this paper introduces the two  
65 separate QC methods used sequentially to mask erroneous data records (Sect. 4). We then present  
66 examples of time series of meteorological variables in northwest Greenland, infer their implications



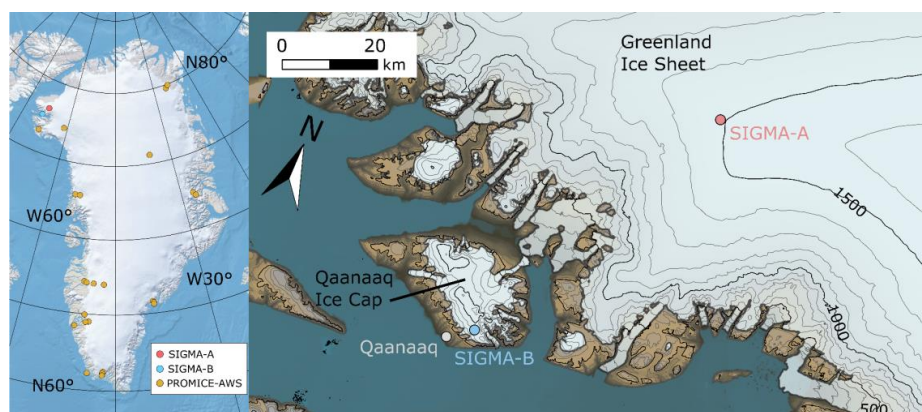
67 for interannual variations in weather conditions, and describe the differences between the two sites  
68 (Sect. 5).

## 69 2. Site description

70 The two AWSs are installed at the SIGMA-A site ( $78.052^\circ$  N,  $67.628^\circ$  W; 1490 m a.s.l.), on the  
71 northwest Greenland Ice Sheet, and the SIGMA-B site ( $77.518^\circ$  N,  $69.062^\circ$  W; 944 m a.s.l.), on the  
72 Qaanaaq Ice Cap, a peripheral ice cap on the Greenland coast (Fig. 1). They have been in operation  
73 since July 2012 (Aoki et al., 2014).

74 The SIGMA-A site is 70 km inland from the coast on a ridge of the Greenland Ice Sheet extending  
75 northwest from the Greenland Summit; it sits on a flat snow surface with no obstacles around the site  
76 (see Fig. 2). It is considered to be in an accumulation area for the ice sheet (Matoba et al., 2018) based  
77 on the analysis of ice-core data (Yamaguchi et al., 2014; Matoba et al., 2017). The SIGMA-B site is 3  
78 km north of the village of Qaanaaq. Its location is supposed to be near the equilibrium line (910 m  
79 a.s.l.; Tsutaki et al., 2017) on the Qaanaaq Ice Cap, which ranges in elevation between 30 and 1110 m  
80 a.s.l. (Sugiyama et al., 2014). The surface condition at this site varies (see Fig. 2), and surface melting  
81 has occurred in warm years (e.g., Aoki et al., 2014). The site is on a southwest-facing slope (azimuth  
82  $220^\circ$ ) with an angle of  $4^\circ$  according to 10 m DEM data (Porter et al., 2018).

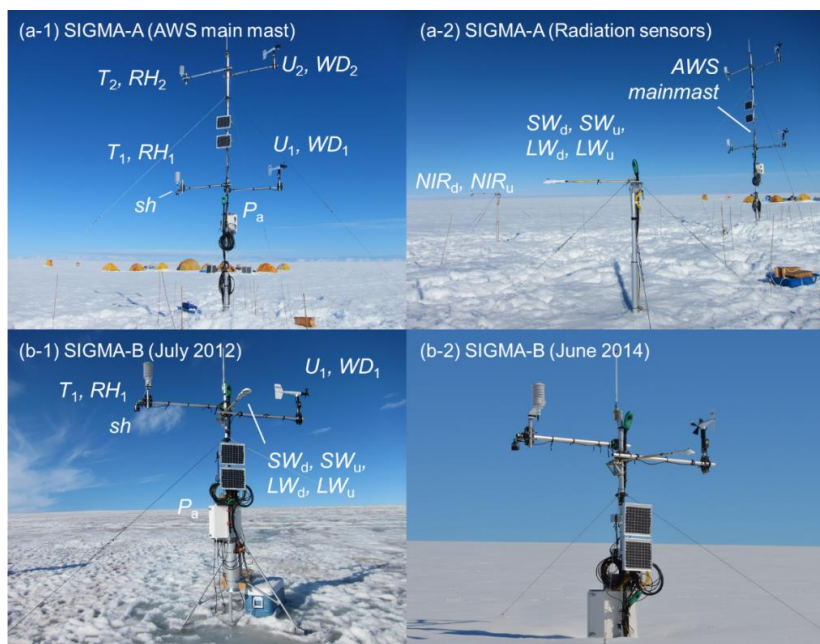
83



84

85 Figure 1. Location map of Greenland showing AWS sites (left) and a local map of northwest Greenland  
86 showing locations of AWS sites SIGMA-A and SIGMA-B. Contour interval in the right panel is 100  
87 m.

88



89

90 Figure 2. Setting and instrumentation at the SIGMA-A site (top) and the SIGMA-B site (bottom).  
91 Surface conditions at SIGMA-B are shown in July 2012 and June 2014. Sensors are labeled with the  
92 observation parameters they measure (see Table 1).

93

### 94 3. Description of AWS systems and datasets

#### 95 3.1. Specifications

96 Sensor specifications for the meteorological observations are listed in Table 1, and overviews of  
97 the two AWS systems are shown in Fig. 2. Each AWS mainmast is set in a hole drilled using a hand  
98 auger. Sensors for air temperature, relative humidity, and wind speed and direction are mounted at the  
99 ends of horizontal poles to exclude possible thermal and wind disturbances from the mainmast. The  
100 SIGMA-A sensors are placed 3 m and 6 m above the surface, as signified by subscripts “1” (lower)  
101 and “2” (upper) in the corresponding data variables. The SIGMA-B sensors are set at 3 m above the  
102 surface and have subscripts of “1”. The snow height sensor at both sites is mounted at 3 m height  
103 beneath the air temperature and relative humidity sensors. Six snow temperature sensors have been set  
104 as follows. Four sensors were set at 19:00 UTC on 29 June 2012 at depths of 1 m ( $st_1$ ), 0.7 m ( $st_2$ ), 0.4  
105 m ( $st_3$ ), and 0.05 m ( $st_4$ ) under the snow surface. At 21:00 UTC on 27 July 2013, sensors  $st_3$  and  $st_4$   
106 were relocated to depths of 0.46 m and 0.16 m, respectively. Sensors  $st_5$  and  $st_6$  were set at 0.05 m



107 under the surface and 0.45 m above the surface, respectively, at 14:00 UTC on 9 June 2014. Sensors  
 108 for shortwave, longwave, and near-infrared radiation are installed at SIGMA-A on separate poles 10  
 109 m from the mainmast (Fig. 2a-2). A pyranometer and a pyrgeometer at SIGMA-B are mounted on the  
 110 mainmast facing directly south. Tilt angles of the mainmast in the north-south ( $Tilt_x$ ) and east-west  
 111 ( $Tilt_y$ ) directions are monitored with an inclinometer attached to the mainmast. The additional suffix  
 112 “A” or “B” represents the site name in the variables introduced below.

113 Electric power is supplied to the AWS systems by a cyclone battery that is charged constantly by  
 114 solar panels attached to the mainmast. All parameters are recorded once per minute and stored in a  
 115 data logger (C-CR1000, Campbell Scientific, USA), except for the mainmast’s snow height and tilt  
 116 angles, which are recorded every hour. Hourly data are calculated for the other parameters by  
 117 averaging the 1-min data. All hourly data are sent regularly to the data server via the Argos satellite  
 118 channel.

119 Snow height is measured with an ultrasonic snow gauge (Table 1). The raw data from this sensor  
 120 ( $sh_{raw}$ ) is the distance from the sensor to the snow surface, which has a temperature dependence. The  
 121 temperature-corrected snow height ( $sh$ ) is calculated from

$$122 \quad sh = sh_{initial} - sh_{raw} \times \sqrt{\frac{T_2 + 273.15}{273.15}} \times 100, \quad (i)$$

123 where  $sh_{initial}$  (= 300 cm) is the initially installed sensor height from the surface and  $T_2$  is air  
 124 temperature.

125

126 Table 1. Meteorological observation parameters and sensor specifications.

127

observation parameter	abbreviation	unit	sensor	observaion range	accuracy
wind speed	$U_n^a$	$m s^{-1}$	Young, 05103	0 to 100 [ $m s^{-1}$ ]	$1.0 m s^{-1 c}$
wind direction	$WD_n^a$	degree	Young, 05103	360° mechanical, 355° electrical (5° open)	$1.1 m s^{-1}$ at 10° displacement <sup>c</sup>
air temperature	$T_n^a$	°C	Vaisala, HMP155 <sup>b</sup>	−80 to +60 [°C]	±0.17 °C
relative humidity	$RH_n^a$	%	Vaisala, HMP155 <sup>b</sup>	0 to 100%	±1% (0 to 90%) ±1.7% (90 to 100%)
atmospheric pressure	$P_a$	hPa	Vaisala, PTB210	500 to 1100 [hPa]	±0.30 hPa at 20 °C
downward and upward shortwave radiation	$SW_\phi, SW_u$	$W m^{-2}$	Kipp & Zonen, CNR4	0.3 to 2.8 [ $\mu m$ ]	5 to 20 $\mu V W^{-1} m^{-2}$
downward and upward longwave radiation	$LW_\phi, LW_u$	$W m^{-2}$	Kipp & Zonen, CNR4	4.5 to 42 [ $\mu m$ ]	5 to 20 $\mu V W^{-1} m^{-2}$
downward and upward near-infrared radiation	$NIR_\phi, NIR_u$	$W m^{-2}$	Kipp & Zonen, CMP6 with a RG715 cut-off filter	0.715 to 2.8 [ $\mu m$ ]	5 to 20 $\mu V W^{-1} m^{-2}$
snow height	$sh$	cm	Campbell, SR50	0.5 to 10 [m]	1 cm or 0.4%
snow temperature	$st_n^a$	°C	Climatec, C-PTWP-10	−40 to +60 [°C]	±0.15°C
tilts of the main mast	$Tilt_x, Tilt_y$	degree	TURCK, B2N85H- Q20L60-	−85° to +85°	±0.5°

a: “n” suffix is appended to distinguish the observation height or depth.

b: protected from direct solar irradiance by a naturally-aspirated 14-plate Gill radiation shield

c: threshold sensitivity

128



129

### 130 3.2. Data processing

131 We describe the calculations for some variables used in the QC process in this section. Table 2  
132 shows the key constants, variables, and abbreviations used in this study.

133 Because the vertical radiant flux against the inclined surface needed to accurately calculate the  
134 surface albedo and surface energy balance is affected by the sloping surface at the SIGMA-B site, we  
135 calculated the slope-corrected downward shortwave radiation ( $SW_{d\_slope}$ ) from the corresponding  
136 observations using the correction method in Jonsell et al. (2003) and Hock and Holmgren (2005). The  
137  $SW_{d\_slope}$  is calculated by

$$138 \quad SW_{d\_slope} = I_s + I_d, \quad (ii)$$

139 where  $I_s$  and  $I_d$  are the direct and diffuse shortwave radiation for a slope, respectively:

$$140 \quad I_s = SW_d \times d, \quad (iii)$$

$$141 \quad I_d = SW_d \times (1 - d) \times \frac{\cos \theta_{slope}}{\cos \theta}, \quad (iv)$$

142 where  $d$  is the ratio of total diffuse radiation to global radiation and  $\theta$  and  $\theta_{slope}$  [radian] are the solar  
143 zenith angle and the solar zenith angle for a slope, respectively. The ratio  $d$  is obtained from  
144 atmospheric transmittance  $t_r$  by

$$145 \quad d = \begin{cases} 0.15 & \text{for } 0.8 \leq t_r, \\ 0.929 + 1.134t_r - 5.111t_r^2 + 3.106t_r^3 & \text{for } 0.15 < t_r < 0.8, \\ 1.0 & \text{for } t_r \leq 0.15, \end{cases} \quad (v)$$

146 where

$$147 \quad t_r = \frac{SW_d}{SW_{TOA}}, \quad (vi)$$

148 where  $SW_{TOA}$  is the downward shortwave radiation at the top of the atmosphere, calculated by

$$149 \quad SW_{TOA} = I_0 \left( \frac{r_m}{r} \right)^2 \cos \theta, \quad (vii)$$

150 where  $I_0$  ( $= 1361 \text{ W m}^{-2}$ ) is the solar constant (Rottman, 2006; Fröhlich, 2012),  $r$  is the distance  
151 between the Sun and the Earth (assuming an elliptical orbit with an eccentricity of 0.01637), and  $r_m$  is  
152 its annual mean ( $= 1.496 \times 10^8 \text{ km}$ ).

153 The solar zenith angle for a slope in Eq. (iv) is calculated by

$$154 \quad \cos \theta_{slope} = \cos \beta \cos \theta + \sin \beta \sin \theta \cos(\varphi - \varphi_{slope}), \quad (viii)$$

155 where  $\beta$  is the slope angle from a horizontal plane, and  $\varphi$  and  $\varphi_{slope}$  are the solar azimuth and the solar  
156 azimuth for the slope direction, respectively. Solar zenith and azimuth angles are calculated from the  
157 geographic position of the observation site and the date and time.

158 Shortwave and near-infrared albedos ( $\alpha_{sw}$  and  $\alpha_{nir}$ , respectively) are calculated as the ratio of



159 upward and downward radiant fluxes, as shown for  $\alpha_{sw}$  by

$$160 \quad \alpha_{sw} = \frac{SW_u}{SW_d}, \quad (ix)$$

161 where  $SW_u$  is the upward shortwave radiant flux and  $SW_d$  is the downward shortwave radiant flux. The  
162 daily integrated shortwave albedo ( $\alpha_{sw,i}$ ) is calculated as the ratio of cumulative upward and  
163 downward radiant fluxes for the past 24 h:

$$164 \quad \alpha_{sw,i} = \frac{\sum_{24h} SW_u}{\sum_{24h} SW_d}. \quad (x)$$

165 The near-infrared albedo ( $\alpha_{nir}$ ) and daily integrated near-infrared albedo ( $\alpha_{nir,i}$ ) are calculated in the  
166 same way. The near-infrared fraction is the ratio of the downward near-infrared radiant flux ( $NIR_d$ ) to  
167  $SW_d$ .

168

169 Table 2. Key constants, variables, and their symbols used in this paper.



symbol	name	value	unit
constant			
$f_{sp}$	a fraction of near-infrared radiant flux in the shortwave radiant flux at the top of the atmosphere	0.5151	no dimension
$I_0$	solar constant	1361	W m <sup>-2</sup>
$n$	cloud cover coefficient	0.5	no dimension
$r_m$	annual mean distance between the Sun and the Earth	$1.496 \times 10^8$	km
$sh_{\text{obsA}}$	initial height of the snow height sensor	300	cm
$\kappa$	constant depending on cloud type	0.26	no dimension
$\varepsilon$	snow/ice surface emissivity	0.98	no dimension
$\sigma$	Stefan-Boltzmann constant	$5.67 \times 10^8$	W m <sup>-2</sup> K <sup>-4</sup>
variable			
$d$	diffuse fraction in global radiation		no dimension
$I_d$	diffuse solar radiation		W m <sup>-2</sup>
$I_d$	direct solar radiation		W m <sup>-2</sup>
$LW_d$	downward longwave radiation		W m <sup>-2</sup>
$LW_{\text{atm}}$	standard atmospheric longwave radiation		W m <sup>-2</sup>
$LW_u$	upward longwave radiation		W m <sup>-2</sup>
$NIR_d$	downward near-infrared radiation		W m <sup>-2</sup>
$NIR_u$	upward near-infrared radiation		W m <sup>-2</sup>
$P_s$	atmospheric pressure		hPa
$r$	distance between the Sun and the Earth		m
$RH_{1,2}^a$	relative humidity		%
$sh$	snow height		cm
$sh_{\text{raw}}$	raw data of snow height		m
$solz$	solar zenith angle		degree
$solz_{\text{slope}}$	solar zenith angle for a slope		degree
$st_{1,2}^b$	snow temperature		°C
$st\_depth_{1,2}^b$	snow temperature sensor depth		m
$SW_d$	downward shortwave radiation		W m <sup>-2</sup>
$SW_{d,\text{slope}}$	downward shortwave radiation for a slope		W m <sup>-2</sup>
$SW_{\text{atm}}$	downward shortwave radiation at the top of the atmosphere		W m <sup>-2</sup>
$SW_u$	upward shortwave radiation		W m <sup>-2</sup>
$T_r$	transmissivity of the atmosphere for shortwave radiation		no dimension
$T_{1,2}^a$	air temperature		°C
$WD_{1,2}^a$	wind direction		degree
$U_{1,2}^a$	wind speed		m s <sup>-1</sup>
$\alpha_{\text{sw}}$	surface albedo		no dimension
$\alpha_{\text{sw},1}$	daily integrated surface albedo		no dimension
$\alpha_{\text{sw},2}$	surface near-infrared albedo		no dimension
$\alpha_{\text{sw},1}$	daily integrated surface near-infrared albedo		no dimension
$\beta$	slope angle		radian
$\varepsilon_0$	clear-sky atmospheric emissivity		no dimension
$\varepsilon^*$	atmospheric emissivity		no dimension
$\theta$	solar zenith angle		radian
$\theta_{\text{slope}}$	solar zenith angle for a slope		radian
$\phi$	solar azimuth angle		radian
$\phi_{\text{slope}}$	solar azimuth angle of a slope		radian

<sup>a</sup> 1: observed at lower height, 2: observed at upper height (only at the SIGMA-A site)

<sup>b</sup> 1-6: observing depth

170

171





## 172 **4. Quality control**

173 The datasets of observations at sites SIGMA-A and SIGMA-B are classified into four QC levels  
174 numbered 1.0 to 1.3. A Level 1.0 dataset, which is not archived in any repository, is a raw dataset  
175 without data processing. A Level 1.1 dataset is a raw dataset with flags added to indicate missing data  
176 for periods when the data logger was inoperative. A Level 1.2 dataset has undergone an initial control,  
177 which uses a simple masking algorithm to eliminate anomalous values that violate physical laws or  
178 are impossible in the observed environment. The initial control improves the accuracy of the statistical  
179 processing that follows and reduces the possibility of excluding true values. A Level 1.3 dataset has  
180 undergone a secondary control, in which statistical methods are used on Level 1.2 data to identify and  
181 mask outlier values. It has also undergone a final manual masking procedure, in which a researcher  
182 visually checks the dataset and masks outliers based on subjective criteria.

183 The initial control method is described in Sect. 4.1 and the secondary control method is described  
184 in Sect. 4.2. In these sections, the parameter suffixes related to the differences in observation height  
185 (1 and 2) and sites (A and B) are omitted except when needed for clarity. Erroneous records are flagged  
186 with one of the following numerical expressions to signify the reason they have been flagged:

187 –9999: a missing or erroneous data record attributed to a mechanical malfunction or a local  
188 phenomenon such as sensor icing, riming, or burial in snow.

189 –9998: an erroneous radiation record when the radiant sensor was covered with snow or frost.

190 –9997: a record of snow temperature sensor depth when the sensor was suspected to be located above,  
191 not below the snow surface.

192 –8888: a record flagged during the manual masking procedure.

### 193 **4.1. Initial QC for Level 1.2 datasets**

194 The objectives of the initial control are to eliminate erroneous records due to mechanical  
195 malfunctions or local phenomena and pre-treat Level 1.1 datasets for the secondary control. The initial  
196 control consists of a range test (e.g., Fiebrich et al., 2010; Estévez et al., 2011) and a manual mask  
197 procedure. The range test sets variation ranges for each observed parameter in northwest Greenland  
198 on the basis of simple statistics (maximum, minimum, and mean values) derived from records in the  
199 Level 1.1 dataset during a period with no obvious erroneous data. Records outside this statistical range  
200 are flagged with a “–9999” code. Table 3 lists the parameters subjected to this test and their assigned  
201 ranges. The manual masking procedure identified specific erroneous values that resulted from an  
202 electrical malfunction and flagged them with a “–8888” code. The following subsections offer detailed  
203 and additional explanations of the initial control.



#### 204 4.1.1. Wind speed and wind direction

205 The ranges for wind speed ( $U_n$ ) and wind direction ( $WD_n$ ) were set at

$$206 \quad 0 < U_n < U_{\max} + 15.0, \quad (1.1.1)$$

$$207 \quad 0 < WD_n \leq 360. \quad (1.1.2)$$

208  $U_{\max}$  is the maximum value between the beginning of observation and 31 August 2020, and +15.0 m  
209  $s^{-1}$  was taken as the range margin for the upper limit of  $U_n$ . No data points for  $U_n$  were flagged by this  
210 initial control; however, the secondary control added a further condition that flagged erroneous values.

211 When  $U_n$  was zero (no wind),  $WD_n$  was flagged as erroneous:

$$212 \quad U_n = 0 \text{ and } WD_n > 0 \rightarrow WD_n \text{ flagged } -9999. \quad (1.1.3)$$

213 When  $WD_n$  had a negative value, it was modified to zero:

$$214 \quad WD_n \leq 0 \rightarrow WD_n = 0. \quad (1.1.4)$$

#### 215 4.1.2. Air temperature and relative humidity

216 The ranges for air temperature ( $T_n$ ) and relative humidity ( $RH_n$ ) were set at

$$217 \quad T_{n_{\min}} - 10.0 < T_n < T_{n_{\max}} + 10.0, \quad (1.2.1)$$

$$218 \quad 0 \leq RH_n \leq 100. \quad (1.2.2)$$

219  $T_{n_{\max}}$  and  $T_{n_{\min}}$  were determined from the observation period ending 31 August 2020. The range  
220 margin for  $T_n$  was set as  $\pm 10.0$  °C. Discrepancies arising from the dual sensors at SIGMA-A were  
221 addressed in the secondary control (see Sect. 4.2.2).

#### 222 4.1.3. Shortwave and near-infrared radiation

223 The main objective of the initial control for shortwave radiation was to mask erroneous records  
224 attributed to electrical noise. The range test is based on the assumption that  $SW_d$  cannot exceed the  
225 maximum of  $SW_{TOA}$  ( $SW_{TOA_{\max}}$ ) during the observation period ( $761.6 \text{ W m}^{-2}$  at SIGMA-A and  $772.2$   
226  $\text{W m}^{-2}$  at SIGMA-B), and albedos  $\alpha_{sw}$  and  $\alpha_{nir}$  cannot be lower than 0.95 and 0.90, respectively,  
227 as determined from the radiative transfer model calculation (Aoki et al., 2003). Moreover, the fraction  
228 of the near-infrared spectral domain at the top of the atmosphere ( $f_{nir}$ ) is assumed to be equal to 0.5151  
229 based on the extraterrestrial spectral solar radiation (Wehrli, 1985). Based on those assumptions,  
230 upward and downward radiation fluxes were flagged as erroneous ( $-9999$ ) according to the following  
231 criteria:

$$232 \quad SW_d < SW_{TOA_{\max}}, \quad (1.3.1)$$

$$233 \quad NIR_d < f_{nir} SW_{TOA_{\max}}, \quad (1.3.2)$$

$$234 \quad SW_u < 0.95 SW_{TOA_{\max}}, \quad (1.3.3)$$

$$235 \quad NIR_u < 0.90 f_{nir} SW_{TOA_{\max}}. \quad (1.3.4)$$

236 The following procedures were also applied to mask erroneous records due to electrical noise.



237 These parameters were flagged as erroneous (−9999) when  
238  $(SW_d, SW_u, NIR_d, NIR_u) < 0$  and  $solz < 90.0$ , (1.3.4)

239 and were changed to zero when  
240  $(SW_d, SW_u, NIR_d, NIR_u) < 0$  and  $solz \geq 90.0$ . (1.3.5)

#### 241 4.1.4. Longwave radiation

242 The ranges for  $LW_d$  and  $LW_u$  were set as follows:

$$243 \quad 0 < LW_d (LW_u) < LW_{d\_max} (LW_{u\_max}), \quad (1.4.1)$$

244 where

$$245 \quad LW_{d\_max} = \varepsilon_{max} \sigma T_{2A\_max} (T_{1B\_max}), \quad (1.4.2)$$

$$246 \quad LW_{u\_max} = \varepsilon \sigma T_{s\_max}. \quad (1.4.3)$$

247 Maximum values were determined under the following assumptions: (1)  $T_{2A}$  and  $T_{1B}$  cannot be larger  
248 than  $T_{2A\_max}$  and  $T_{1B\_max}$ , respectively, (2) atmospheric emissivity is set to unity ( $\varepsilon_{max}$ ), and (3) the value  
249 of  $LW_{u\_max}$  is determined by assuming that the surface temperature cannot exceed  $T_{s\_max}$  (= 10 °C),  
250 which includes errors due to longwave emissions from the poles of the AWS system and similar  
251 sources, and that the emissivity of the snow/ice surface ( $\varepsilon$ ) is 0.98 (Armstrong and Brun, 2008).

252 Both upward and downward longwave fluxes were considered erroneous when the sensor appeared  
253 to be covered with snow or frost:

$$254 \quad |LW_d - LW_u| \leq 1.0 \rightarrow LW_d \text{ and } LW_u \text{ flagged } -9998. \quad (1.4.4)$$

#### 255 4.1.5. Snow height

256 The range test for snow height ( $sh$ ) was imposed separately for each period between maintenances  
257 to the SIGMA-A site, when the mainmast extension was adjusted to prevent the sensors from being  
258 buried in snow. (A single range test sufficed for SIGMA-B.) For each test, the range was set so that  $sh$   
259 varied from the median by  $\pm 100$  cm or  $\pm 150$  cm, a margin that was determined depending on the  
260 variation of the data records in each period. The objective was to mask the most obvious outliers. In  
261 addition, corrections were made to the  $sh$  records after each of three maintenance visits to the AWS at  
262 SIGMA-A.

#### 263 4.1.6. Atmospheric pressure

264 The range test for atmospheric pressure ( $P_a$ ) was conducted according to

$$265 \quad P_{a\_ave} - 100.0 < P_a < P_{a\_ave} + 100.0, \quad (1.6.1)$$

266 where  $P_{a\_ave}$  is the average atmospheric pressure for the observation period at each AWS site (Table  
267 3). The additional margin that defined the range was  $\pm 100$  hPa.



268 **4.1.7. Snow temperature**

269 The range test for snow temperature ( $st_n$ ) was conducted according to

270 
$$T_{1\_min} < st_n < 0.2, \quad (1.7.1)$$

271 where  $T_{1\_min}$  is the minimum air temperature for the site and the upper threshold, 0.2 °C, incorporates  
 272 the sensor's absolute error of 0.15 °C and the requirement that the snow temperature cannot be positive.

273

274 Table 3. Threshold values used in the range tests, determined from the entire observation period up to  
 275 31 August 2020.

meteorological parameter	unit	threshold value			
		SIGMA-A		SIGMA-B	
		parameter name	value	parameter name	value
wind speed	$\text{m s}^{-1}$	$U_{1A\_max}$	23.9	$U_{1B\_max}$	21.9
		$U_{2A\_max}$	25.5	–	–
air temperature	°C	$T_{1A\_max}$	7.2	$T_{1B\_max}$	10.7
		$T_{2A\_max}$	7.2	–	–
		$T_{1A\_min}$	–49.9	$T_{1B\_min}$	–40.5
		$T_{2A\_min}$	–49.9	–	–
longwave radiation	$\text{W m}^{-2}$	$LW_{dA\_max}$	418.8	$LW_{dB\_max}$	440.1
		$LW_{uA\_max}$	357.2	$LW_{uB\_max}$	357.2
atmospheric pressure	hPa	$P_{a\_aveA}$	833.1	$P_{a\_aveB}$	894.2

276

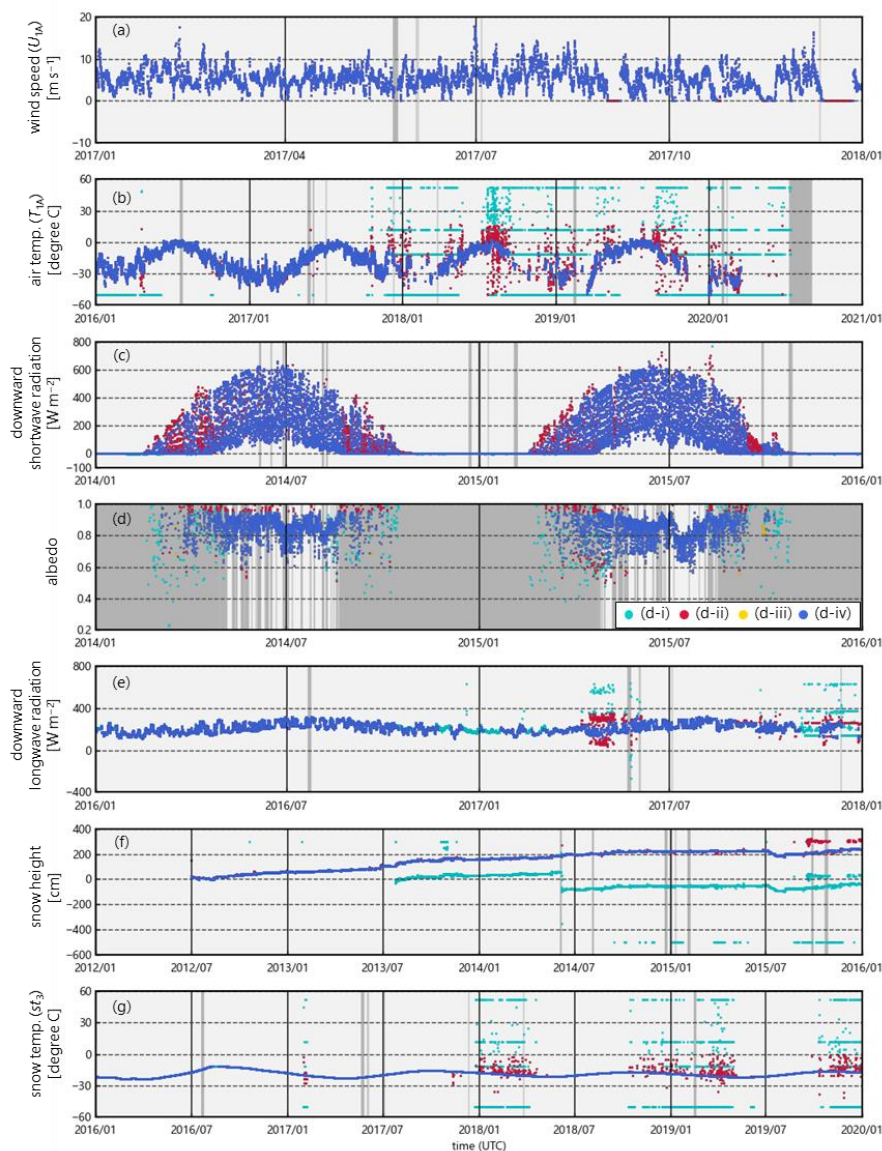
277

278 **4.2. Secondary QC for Level 1.3 datasets**

279 The secondary control applies another range test, an anomaly test, and a manual mask procedure.

280 The range test, applied only to the shortwave radiation and albedo data, sets a more precise variation  
 281 range than the initial control and masks erroneous data records. The anomaly test sets a median and  
 282 standard deviation (SD), which govern statistical tests used to determine the possible range of normal  
 283 values in the Level 1.2 dataset and identify and mask outliers. The manual mask procedure identifies  
 284 and masks any remaining erroneous records. The effects of the initial and secondary controls are  
 285 illustrated in Fig. 3 and described in detail below. .

286



287

288 Figure 3. Examples of the initial and secondary controls for the SIGMA-A site: (a) wind speed ( $U_{1A}$ ),  
 289 (b) air temperature ( $T_{1A}$ ), (c) downward shortwave radiation, (d) surface albedo, (e) downward  
 290 longwave radiation, (f) snow height, and (g) snow temperature ( $st_3$ ). In all panels except (d), the dark  
 291 gray areas represent time periods in which data records in the Level 1.0 dataset were masked to  
 292 produce the Level 1.1 dataset, light blue dots denote records masked by the initial control, red dots



293 denote records masked by the secondary control, and dark blue dots are the Level 1.3 data records. In  
294 panel (d), the gray shaded area represents the masked (−9999) data records that cannot be calculated  
295 due to the absence of, masked  $SW_d$ , or for other reasons. The light blue, red and yellow dots represent  
296 data points masked by three QC operations during the secondary control; see Sect. 4.2.4 for  
297 explanation.

#### 298 4.2.1. Wind speed and wind direction

299 When  $U_n$  was zero for more than 6 continuous hours,  $U_n$  and  $WD_n$  were both flagged as erroneous  
300 (−9999) under the assumption that the wind sensor was blocked by snow and ice. Although the initial  
301 control eliminated no  $U_n$  records, this step masked many values in the winter (Fig. 3a).

#### 302 4.2.2. Air temperature and relative humidity

303 Anomaly tests for air temperature and relative humidity were only applied to the lower-level  
304 sensor records for SIGMA-A (i.e.,  $T_{1A}$  and  $RH_{1A}$ ). The anomaly test compared the difference  
305 ( $\Delta T$  and  $\Delta RH$ ) between readings of the upper and lower sensors (i.e.,  $|T_{1A} - T_{2A}|$  and  $|RH_{1A} -$   
306  $RH_{2A}|$ ) to the respective medians and SDs of those parameters:

$$307 \quad \Delta T < \text{median}_{\Delta T} + \text{SD}_{\Delta T} \times 3 \quad \text{for before 1 September 2017,} \quad (2.2.1)$$

$$308 \quad \Delta T < \text{median}_{\Delta T} + \text{SD}_{\Delta T} \quad \text{for after 1 September 2017,} \quad (2.2.2)$$

$$309 \quad \Delta RH < \text{median}_{\Delta RH} + \text{SD}_{\Delta RH} \times 3. \quad (2.2.3)$$

310 The medians were calculated from the data before 1 September 2017, because the data after that date  
311 appeared to include many erroneous  $T_{1A}$  records due to deterioration of the data logger or sensor. For  
312 these later records, the SD criterion was adjusted to more stringently detect outliers in the records of  
313  $T_{1A}$  and  $RH_{1A}$ , which were flagged as erroneous (−9999). The effectiveness of this adjustment is clear  
314 in Fig. 3b.

#### 315 4.2.3. Shortwave and near-infrared radiation

316 The anomaly test for shortwave and near-infrared radiation was intended to mask the noise  
317 resulting from a weak electric pulse at large solar zenith angles. The median and SD values were  
318 calculated from only the records ( $SW_d$ ,  $SW_u$ ,  $NIR_d$ , and  $NIR_u$ ) at  $solz > 90.0^\circ$  to distinguish this noise  
319 source according to the following, using  $SW_d$  as an example:

$$320 \quad SW_d < \text{median}_{SW_d} + \text{SD}_{SW_d} \times 3. \quad (2.3.1)$$

321 Records identified as noise were modified to zero.

322 The downward radiation components were sometimes overestimated as a result of icing or riming  
323 over the glass dome of the pyranometer. To mask these erroneous values, we applied range tests based  
324 on  $SW_{TOA}$  and a threshold value of atmospheric transmittance  $T_t$  (0.881 for SIGMA-A and 0.872 for



325 SIGMA-B) calculated by a radiative transfer model (Aoki et al., 1999, 2003):

$$326 \quad SW_d < T_r SW_{TOA}, \quad (2.3.2)$$

$$327 \quad NIR_d < T_r f_{nir} SW_{TOA}. \quad (2.3.3)$$

328 Values of  $SW_d$  and  $NIR_d$  that were outside this range were flagged as erroneous (−9999).

329 To recognize other instances when the radiation sensor was covered with snow or frost,  $SW_d$  and  
330  $NIR_d$  records corresponding to the following case were flagged as erroneous (−9998):

$$331 \quad SW_d(NIR_d) < SW_u(NIR_u). \quad (2.3.4)$$

332 Figure 3c shows that the initial control eliminated a few erroneous  $SW_d$  data recorded in August 2015,  
333 whereas the secondary control masked many records, especially in February–May, that were affected  
334 by riming or frost.

#### 335 4.2.4. Shortwave and near-infrared albedo

336 We calculated albedos  $\alpha_{sw}$  and  $\alpha_{nir}$ , and the statistical values used in all QC procedures for  
337 those albedos, from the  $SW_d$  and  $NIR_d$  datasets that had first undergone secondary control. This  
338 calculation was done in four separate steps, shown by the color of dots in Fig. 3d.

##### 339 (1) Flagging for low pyranometer sensitivity

340 At solar zenith angles near  $90.0^\circ$ ,  $SW_d$  and  $NIR_d$  may not be an accurate measurement because of  
341 the low sensitivity of the pyranometer. We therefore masked  $\alpha_{sw}$  and  $\alpha_{nir}$  values at  $solz > 85.0^\circ$  or  
342 when the  $SW_d$  ( $NIR_d$ ) value was below the median  $SW_d$  ( $NIR_d$ ) value for  $solz > 85.0^\circ$ . Records masked  
343 in this step are shown in Fig. 3d as light blue dots (d-i).

##### 344 (2) Range test for cold and warm periods

345 The range test used the upper and lower thresholds for  $\alpha_{sw}$  and  $\alpha_{nir}$ , as determined by the  
346 radiative transfer calculation of Aoki et al. (2003, 2011) plus a small error margin. Those thresholds  
347 correspond to the assumed surface conditions during two parts of the year. For the cold period of  
348 October–April, we used the following thresholds for different snow or ice conditions:

$$349 \quad 0.6 < \alpha_{sw} < 0.95 \quad \text{for dry snow at SIGMA-A,} \quad (2.4.1)$$

$$350 \quad 0.5 < \alpha_{nir} < 0.90 \quad \text{for dry snow at SIGMA-A,} \quad (2.4.2)$$

$$351 \quad 0.4 < \alpha_{sw} < 0.95 \quad \text{for dry or wet snow at SIGMA-B.} \quad (2.4.3)$$

352 For the warm period of May–September we used the following thresholds:

$$353 \quad 0.4 < \alpha_{sw} < 0.95 \quad \text{for wet snow at SIGMA-A,} \quad (2.4.4)$$

$$354 \quad 0.3 < \alpha_{nir} < 0.90 \quad \text{for wet snow at SIGMA-A,} \quad (2.4.5)$$

$$355 \quad 0.1 < \alpha_{sw} < 0.95 \quad \text{for wet snow or dark ice at SIGMA-B.} \quad (2.4.6)$$

356 Records with albedo values beyond these theoretical thresholds were masked.

##### 357 (3) Anomaly test in low atmospheric transmittance condition

358 The range test was augmented by an anomaly test to identify underestimates of  $\alpha_{sw}$  and  $\alpha_{nir}$   
359 when  $SW_d$  ( $NIR_d$ ) was low and atmospheric transmittance ( $t_r$ ) was small, typically at large solar zenith



360 angles. Whereas the first QC step in this phase used a criterion of  $solz > 85.0^\circ$ , we relaxed it to  $solz >$   
361  $80.0^\circ$  and masked  $\alpha_{sw}$  ( $\alpha_{nir}$ ) values that were unnaturally low owing to low  $t_r$  and  $SW_d$  ( $NIR_d$ ). Data  
362 records that were masked in either the range or anomaly tests are shown in Fig. 3d as red dots (d-ii).

363 (4) Final steps

364 In cases where  $LW_d$  was flagged as “-9998” during the initial control (see Sect. 4.1.4),  $\alpha_{sw}$  and  
365  $\alpha_{nir}$  were flagged as “-9999” under the assumption that the radiation sensors were covered with snow  
366 or frost. The final step was a manual mask procedure. Data records that were masked in this phase are  
367 shown in Fig. 3d as orange dots (d-iii), and the final Level 1.3 dataset is displayed as blue dots (d-iv).

#### 368 4.2.5. Longwave radiation

369 The anomaly test for  $LW_d$  and  $LW_u$  was conducted only for the SIGMA-A dataset using a standard  
370 longwave radiant flux ( $LW_{std}$ ), a measure of the amount of longwave radiation from the near-surface  
371 atmosphere that was calculated from the air temperature measurement by Brock and Arnold (2000)

$$372 \quad LW_{std} = \varepsilon^* \sigma (T_{2A} + 273.15)^4, \quad (\text{xi})$$

$$373 \quad \varepsilon^* = (1 + \kappa n) \varepsilon_0, \quad (\text{xii})$$

$$374 \quad \varepsilon_0 = 8.733 \times 10^{-3} \times (T_{2A} + 273.15)^{0.788}, \quad (\text{xiii})$$

375 where  $\varepsilon^*$  is the atmospheric emissivity,  $\sigma$  ( $= 5.670 \times 10^{-8}$ ) is the Stefan–Boltzmann constant,  $\kappa$   
376 ( $= 0.26$ ) is a constant depending on cloud type (Braithwaite and Olsen, 1990),  $n$  is the cloud cover  
377 amount ( $n$ : [0, 1] and set at 0.5 because it could not be determined), and  $\varepsilon_0$  is the clear-sky emissivity.  
378 We assumed that  $LW_{std}$  was a close approximation of the true longwave radiant fluxes and used the  
379 absolute difference between  $LW_{std}$  and  $LW_d$  or  $LW_u$  (i.e.,  $\Delta LW_d$  or  $\Delta LW_u$ ) and its median and SD as  
380 the basis of the anomaly test.

381 Because parts of the  $LW_d$  dataset contained many erroneous records attributed to degradation of  
382 the data logger (see Fig. 3e), we reduced the SD range limit by half for two time periods, 7 April to 7  
383 June 2017 and after 1 September 2017. The resulting criteria were

$$384 \quad \Delta LW_d < \text{median}_{\Delta LW_d} + \text{SD}_{\Delta LW_d} \times 2 \quad \text{for all periods, except} \quad (2.5.1)$$

$$385 \quad \Delta LW_d < \text{median}_{\Delta LW_d} + \text{SD}_{\Delta LW_d} \quad \text{for two subperiods,} \quad (2.5.2)$$

$$386 \quad \Delta LW_u < \text{median}_{\Delta LW_u} + \text{SD}_{\Delta LW_u} \times 2 \quad \text{for all periods.} \quad (2.5.3)$$

387 Records that were outliers under these criteria were flagged as erroneous (-9999). Figure 3e shows  
388 that the initial control (see Sect. 4.1.4) improved this anomaly test’s efficacy, and the secondary control  
389 yielded a clean  $LW_d$  time series.

#### 390 4.2.6. Snow height

391 The anomaly test for snow height masked data that displayed unrealistic fluctuations.  
392 Differences ( $\Delta sh$ ) were determined with respect to mean and SD values from the preceding 72 h values  
393 during period 1, before 1 September 2017 ( $sh_{\text{mean}1}$ ) and period 2, after 1 September 2017 ( $sh_{\text{mean}2}$ ). The





394 difference between the two periods is that means were not calculated when the 72 h period included  
395 more than 48 flagged records in period 1 and more than 60 flagged records in period 2. The  $\Delta sh$   
396 values were compared to the median plus SD of  $\Delta sh$  for that period. In addition, because snow height  
397 increased steadily in period 2, we derived the regression equation for this increase and identified  
398 outliers with respect to the SD of the regression, i.e.  $\Delta sh_{reg}$ . The resulting criteria were

$$399 \quad \Delta sh_{mean1} < median_1 \Delta sh + SD_1 \Delta sh, \quad (2.6.1)$$

$$400 \quad \Delta sh_{reg} < SD_{reg-sh} \quad \text{for after 1 September 2017,} \quad (2.6.2)$$

$$401 \quad \Delta sh_{mean2} < median_2 \Delta sh + SD_2 \Delta sh \times 3 \quad \text{for after 1 September 2017.} \quad (2.6.3)$$

402 Records of  $sh$  that varied beyond these threshold values were flagged as erroneous (–9999).

403 A manual mask procedure was added as a final step. The result of QC procedure is shown in Fig.  
404 3f. The initial control, which corrected gaps resulting from the AWS maintenance (see Sect. 4.1.5),  
405 yielded the smoothed data record that enabled the application of the anomaly test.

#### 406 4.2.7. Snow temperature

407 In the first step, data records were masked when the snow temperature sensor was suspected to be  
408 located above the snow surface:

$$409 \quad st\_depth_n < -1.0 \rightarrow st_n \text{ flagged } -9999. \quad (2.7.1)$$

410 where  $st\_depth_n$  was calculated using snow height data and the initial setting depth of sensor “n” (see  
411 Sect. 3). The threshold of  $st\_depth_n$  included a margin of 1.0 cm to reflect the accuracy of the snow  
412 height sensor. The  $st_n$  was flagged as “–9997” if we could not judge whether the snow temperature  
413 sensor was located below the snow surface.

414 The anomaly test for  $st_n$  consisted of two procedures. The first procedure relied on a temperature  
415 gap between  $st_4$  and data from each of the other five levels ( $st_{not4}$ ), because  $st_4$  had very few erroneous  
416 data:

$$417 \quad |st_4 - st_{not4}| > median\_st_4 + SD\_st_{not4} \times y. \quad (2.7.2)$$

418 where the multiplier  $y$  is 1, 2, or 3 depending on the intensity of the anomaly variation, and determined  
419 based on the test results in each case.

420 The second procedure used the difference between  $st_n$  and its mean value  $st_{n\_mean}$  from the  
421 previous 72 h, calculated using the same method as  $sh_{mean}$  (see Sect. 4.2.6):

$$422 \quad |st_n - st_{n\_mean}| > median\_st_{n\_mean} + SD\_st_{n\_mean}. \quad (2.7.3)$$

423 In both procedures, the median and SD terms were calculated from records for the full time period.  
424 Records detected as outliers were flagged as “–9999”. Figure 3g shows the results of all procedures,  
425 using  $st_3$  as an example.

#### 426 4.2.8. Atmospheric pressure

427 The time series of  $P_a$  included only a few erroneous records. We masked outliers on the basis of



428  $|P_a - P_{a\_mean}| > 20.0,$  (2.8.1)

429 where  $P_{a\_mean}$  is the average for the past 3 h (excluding masked data records). We set the threshold at  
430 20.0, a higher value than the SD, because using the SD could have masked valid records.

## 431 5. Temporal variations of meteorological parameters

432 This section shows the results of simple analyses of the Level 1.3 dataset.

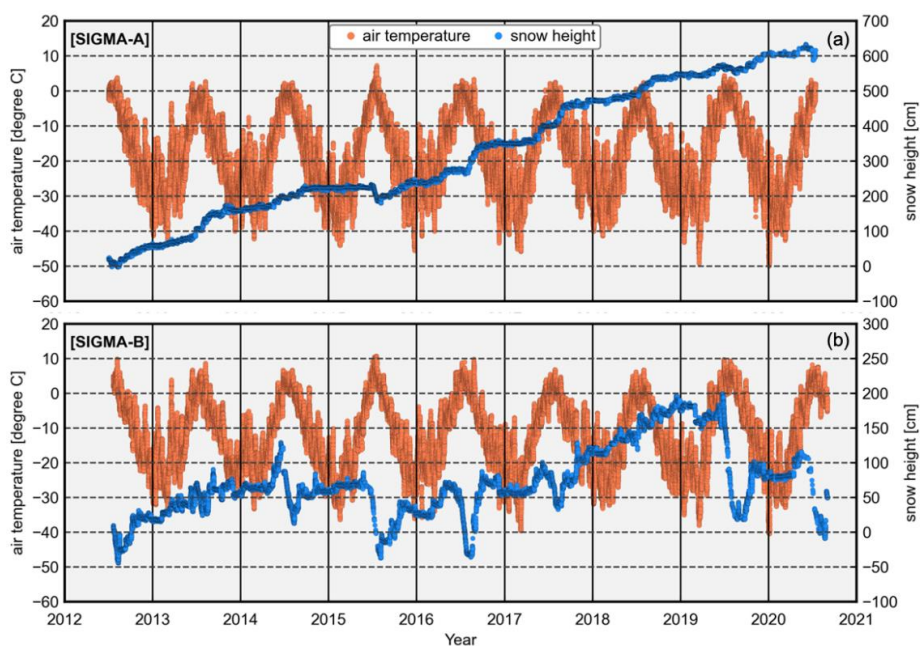
### 433 5.1. Air temperature and snow height

434 Figure 4 shows the air temperature fluctuations and snow height (*sh*) variations at both sites. Mean  
435 air temperatures (2013–2019) were  $-18.1$  °C at the SIGMA-A site and  $-12.3$  °C at the SIGMA-B site.  
436 The annual maxima were recorded every July at both sites, except for August 2019 at the SIGMA-B  
437 site. In contrast, the annual minima occurred in different months between December and March. The  
438 maximum was slightly positive at the SIGMA-A site, and it was above freezing in all years at the  
439 SIGMA-B site. Unusually high temperatures were recorded in mid-July 2015 ( $7.2$  °C at SIGMA-A  
440 and  $10.7$  °C at SIGMA-B). Air temperatures exceeding  $5.0$  °C at SIGMA-A and  $10.0$  °C at SIGMA-B  
441 were common during that period.

442 Warm summers were observed at both sites in 2015, 2016, 2019, and 2020, as indicated by the  
443 cumulative positive degree-day (PDD) records in Fig. 5. PDD generally increased after mid-June and  
444 significantly ascended from late June to July. This tendency was especially strong in warmer years.  
445 PDDs were an order of magnitude greater at SIGMA-B than at SIGMA-A. They increased gradually  
446 until late August at SIGMA-B, whereas the increases at SIGMA-A were stepwise and stopped earlier,  
447 in mid to late July.

448 Snow height steadily increased at the SIGMA-A site during the 8-year study period (Fig. 4), in  
449 which *sh* rose approximately 1 m in the mass-balance years (September to August) of 2013/14,  
450 2016/17, and 2017/18, and decreased slightly in the summers of 2011/12, 2014/15, and 2019/20.  
451 Accumulations were notable in autumn and relatively small in winter. At the SIGMA-B site, in contrast,  
452 increases and decreases in *sh* were observed during each mass-balance year. Decreases in *sh* during  
453 summers were rare during the summers of 2012/13 and 2017/18 but common during the 2013/14,  
454 2014/15, 2015/16, 2018/19, and 2019/20 summers, when decreases were greater than 1 m.

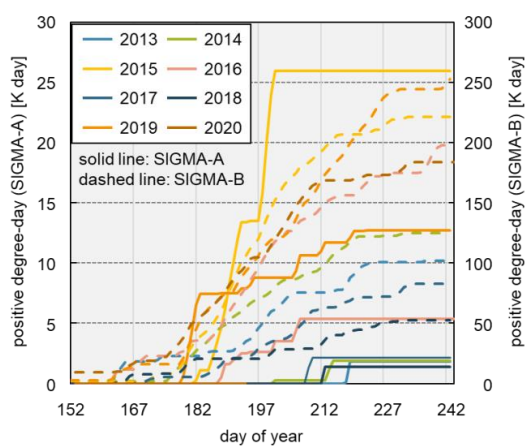
455



456

457 Figure 4. Time series of hourly air temperature and snow height at the (a) SIGMA-A (showing  $T_2$  data)  
458 and (b) SIGMA-B sites.

459



460

461 Figure 5. Cumulative positive degree-days at the SIGMA-A (solid lines) and SIGMA-B (dashed lines)  
462 sites from 1 June to 31 August, 2013–2020.

463

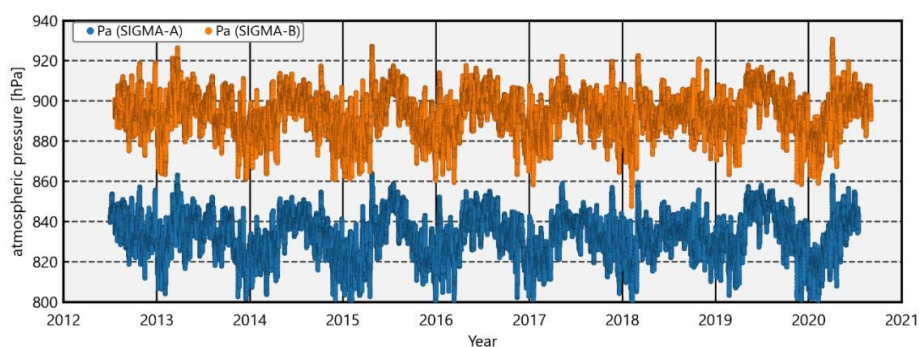


464 **5.2. Atmospheric pressure and seasonal variation of temperature lapse rate**

465 The time series of atmospheric pressure ( $P_a$ ) at the SIGMA-A and SIGMA-B sites show a clear  
466 seasonal variation, high in summer and low in winter (Fig. 6). The two data records had similar  
467 variation patterns that were strongly correlated ( $r = 0.98$ ). The mean values for the whole observation  
468 period were 833.1 hPa at site SIGMA-A and 894.2 hPa at site SIGMA-B (Table 3). The difference in  
469 monthly mean  $P_a$  between the sites was smaller in summer and larger in winter (Fig. 7a), and the  
470 amplitude of the annual cycle was greater at the SIGMA-A site.

471 The apparent lapse rate, indicated by the difference in monthly mean air temperatures between the  
472 elevations of the SIGMA-A and SIGMA-B sites, was approximately  $8 \text{ K km}^{-1}$  in June and July and  
473 approximately  $12 \text{ K km}^{-1}$  in November–February (Fig. 7b). Factors in summer that may contribute to  
474 this seasonal difference include a smaller difference in  $P_a$  between the two sites and moister  
475 atmospheric conditions. The greater annual range of monthly air temperature at site SIGMA-A than at  
476 site SIGMA-B is likely also a winter effect. Winter is colder at SIGMA-A than at SIGMA-B because  
477 the SIGMA-A site is at a higher elevation and farther inland, where cooling by longwave emissions  
478 from the surface is greater and heat advection from the ocean is smaller. The temperature difference  
479 may lead in turn to a larger atmospheric pressure difference between the two sites in winter through  
480 its effect on atmospheric density. The combined summer and winter effects may be the reason that the  
481 apparent lapse rate is greater than the adiabatic reduction rate of the atmosphere (5 K for wet conditions  
482 and 10 K for dry conditions) (Fig. 7b).

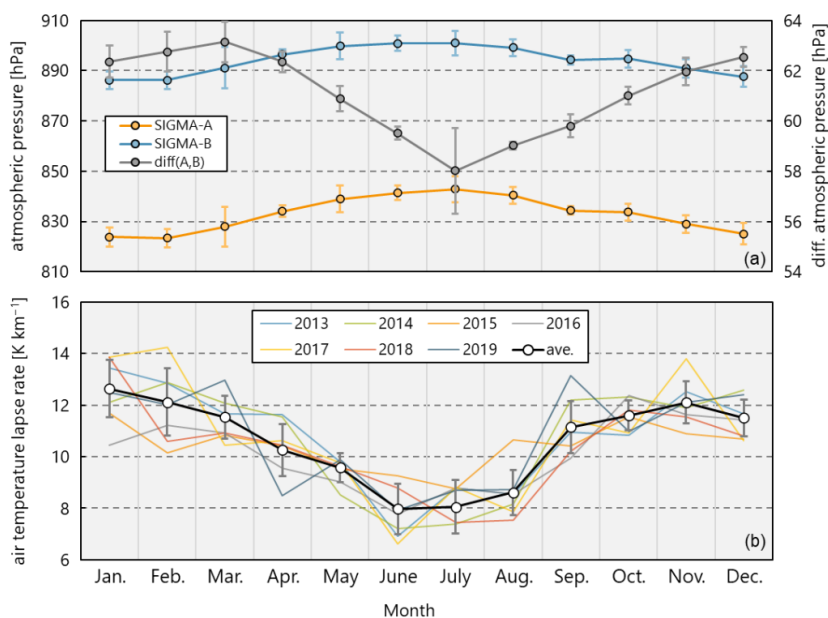
483



484

485 Figure 6. Time series of hourly atmospheric pressure ( $P_a$ ) at the SIGMA-A and SIGMA-B sites.

486



487

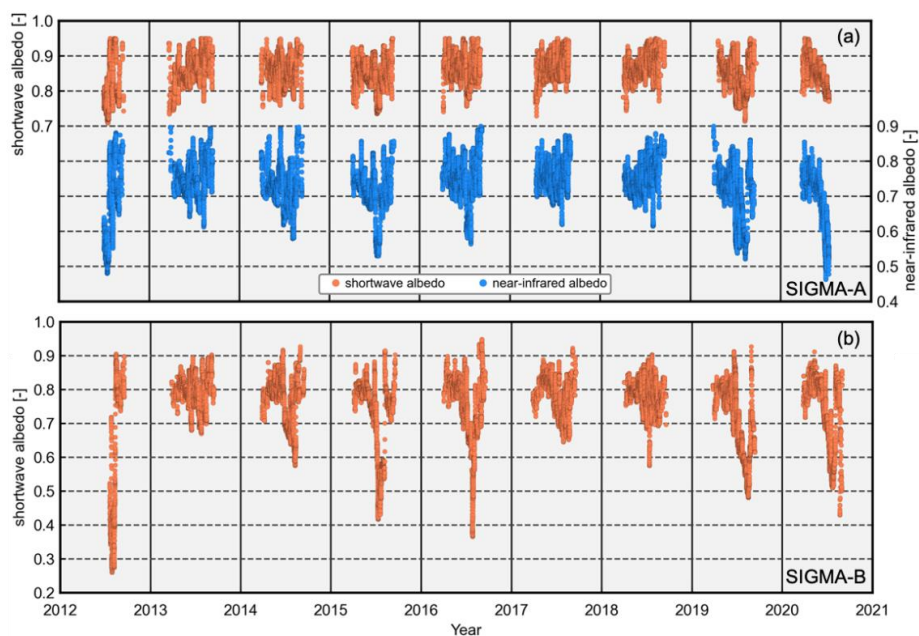
488 Figure 7. Time series of (a) ensemble averages of monthly mean atmospheric pressures during all  
 489 years at both sites and their difference and (b) monthly mean lapse rates of air temperature between  
 490 the SIGMA-A and SIGMA-B sites for each year (colored lines) and their ensemble average during all  
 491 years (open circles). Error bars indicate  $\pm 1$  SD.

492

### 493 5.3. Albedo

494 Whereas shortwave albedo ( $\alpha_{sw}$ ) was rarely lower than 0.7 at site SIGMA-A, near-infrared albedo  
 495 ( $\alpha_{nir}$ ) was below 0.6 in 2012, 2015, 2016, 2019, and 2020 (Fig. 8). Because  $\alpha_{nir}$  depends on the  
 496 snow grain size (Wiscombe and Warren, 1980), this finding implies that snow metamorphism  
 497 progressed at the SIGMA-A site in those years (Hirose et al., 2021). A strong decrease in  $\alpha_{sw}$  was  
 498 observed at the SIGMA-B site during those same summers, which corresponded to notable decreases  
 499 in snow height (Fig. 4b) and high PDDs (Fig. 5). The decreases in albedo may have accelerated  
 500 snowmelt and caused the decreases in snow height at SIGMA-B during the warm summers of those  
 501 years (see Sect. 5.1). It appears that the difference in albedo reduction between the SIGMA-A and  
 502 SIGMA-B sites in summer originated from the difference in air temperature between the sites.

503



504

505 Figure 8. Time series of hourly shortwave and near-infrared albedos at the (a) SIGMA-A and (b)  
506 SIGMA-B sites.

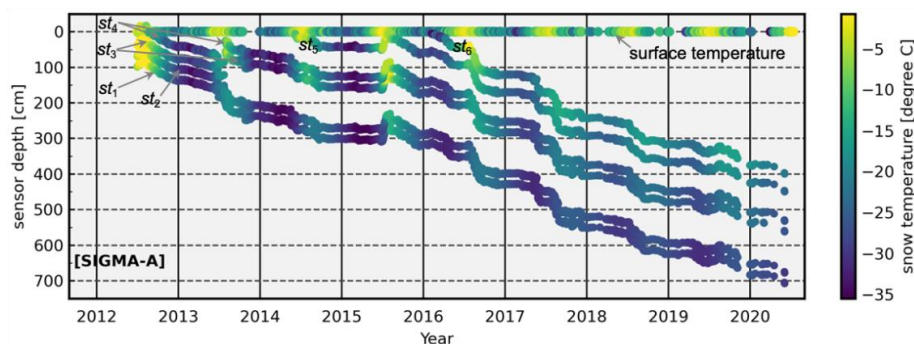
507

#### 508 5.4. Snow temperature

509 Figure 9 shows the time series of snow temperatures ( $st_1$ – $st_6$ ) and snow sensor depths ( $st\_depth_{1-}$   
510  $6$ ). The sensor depths were calculated from each sensor’s initial depths (see Sect. 3.1) and the snow  
511 height variations at the SIGMA-A site. Seasonal and short-term snow temperature fluctuations were  
512 observed, which became smaller after the 2016/17 winter season, when snow accumulation was very  
513 large (Fig. 4). We assumed that the sensors were buried more deeply at that time, resulting in smaller  
514 fluctuations in snow temperature. The annual mean snow temperatures after 2016, a year in which  
515 snow temperatures were relatively stable and less variable, were between  $-18.9 \pm 0.5$  °C ( $st_4$ ) and  
516  $-19.5 \pm 1.7$  °C ( $st_5$ ).

517 Sensors recorded relatively high snow temperatures when they were positioned at shallow depths  
518 below the snow surface. However, in the summer of 2015, sensors  $st_3$  and  $st_4$  registered 0 °C even  
519 though they were more than 1 m below the snow surface. Air temperatures above freezing, and a large  
520 decrease in snow height were observed in this period (Figs. 4 and 5); thus, it is plausible that snowmelt  
521 occurred from the surface to depths near 120 cm, where  $st_3$  was located at that time.

522



523  
524 Figure 9. Time series of hourly snow temperatures ( $st_1$ – $st_6$ ), sensor depth, and surface temperature  
525 (calculated from upward longwave radiation) at the SIGMA-A site.  
526

### 527 5.5. Longwave radiation

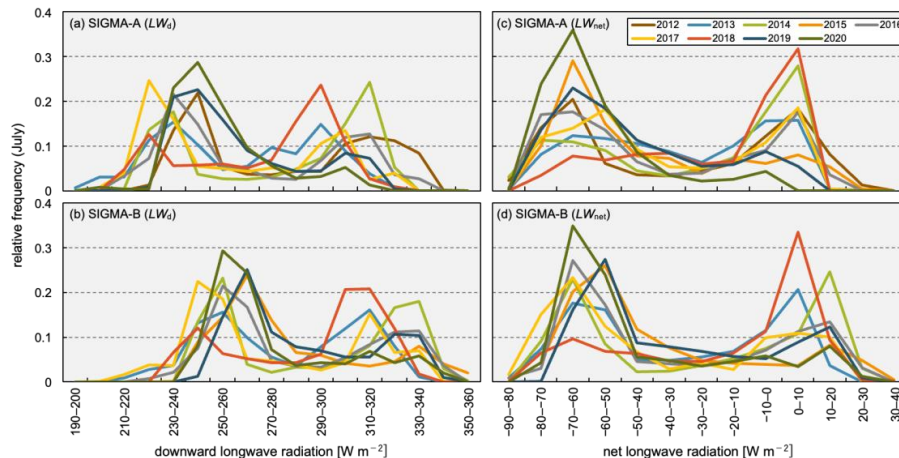
528 The occurrence frequency of longwave radiation, taken to represent the atmospheric condition, is  
529 often used as an indicator of climatological cloudiness (Stramler et al., 2011). Figure 10 shows the  
530 histograms of occurrence frequency of downward ( $LW_d$ ) and net longwave radiation ( $LW_{net} = LW_d -$   
531  $LW_u$ ) during July of all years at the SIGMA-A and SIGMA-B sites. The corresponding histograms for  
532 the four seasons (autumn: SON, winter: DJF, spring: MAM, summer: JJA) are shown in Figs. S1 and  
533 S2. The July  $LW_d$  data from both sites had bimodal distributions, with a lower mode of 220–240  $W$   
534  $m^{-2}$  at SIGMA-A and 240–260  $W m^{-2}$  at SIGMA-B, and a higher mode of 290–310  $W m^{-2}$  at SIGMA-  
535 A and 310–330  $W m^{-2}$  at SIGMA-B. The histograms of July and seasonal  $LW_{net}$  had similar but clearer  
536 bimodal distributions, with modes at approximately 0  $W m^{-2}$  and  $-70 W m^{-2}$  (Figs. 10c-d and S2).

537  $LW_{net}$  can be regarded as an indicator of cloudiness, which can significantly change the downward  
538 longwave radiation and thus the surface temperature of the snow or ice. Both downward and net  
539 longwave radiation increase under overcast conditions because of blackbody radiation from the cloud  
540 cover that is absent in clear-sky conditions. Stramler et al. (2011) and Morrison et al. (2012) have  
541 argued that surface net longwave radiative flux has two modes in occurrence frequency (at  $-40 W m^{-2}$   
542 and 0  $W m^{-2}$ ), which correspond to clear-sky and overcast (low-level mixed-phase clouds) conditions.  
543 In overcast conditions, because the cloud base and the surface are in thermal equilibrium, the vertical  
544 thermal gradient is small and the longwave radiation budget is balanced ( $LW_{net} = 0 W m^{-2}$ ) at the  
545 surface. The two modes of  $LW_{net}$  (0  $W m^{-2}$  and  $-70 W m^{-2}$ ) at the two AWS sites appear to correspond  
546 to the modes proposed by these earlier studies.

547 The occurrence frequency of  $LW_{net}$  in JJA appears to be more variable than those for the other  
548 seasons at both sites (Fig. S2). In these months, the air temperature rises and sea ice extent decreases,  
549 increasing the water vapor supply and advection from the surrounding sea to coastal Greenland (Kim



550 and Kim, 2017; Liang et al., 2022). In such atmospheric conditions, the cloud formation process is  
551 susceptible to synoptic-scale disturbances. The histogram of  $LW_{net}$  for July (Fig. 10) indicates clear-  
552 sky ( $LW_{net} \cong -70 \text{ W m}^{-2}$ ) in 2015, 2019, and 2020 and overcast conditions ( $LW_{net} \cong 0 \text{ W m}^{-2}$ ) in 2014  
553 and 2018. In contrast, annual occurrence frequencies for SON and MAM were less variable than those  
554 for JJA. Overcast and clear-sky conditions dominated in SON and MAM, respectively. Our analysis  
555 shows that cloudiness in JJA was more variable than in other seasons, a result that is also borne out by  
556 satellite observations (Ryan et al., 2022).



557  
558 Figure 10. Histograms of the occurrence frequency of hourly downward longwave radiation ( $LW_d$ ) and  
559 net longwave radiation ( $LW_{net}$ ) observed at the SIGMA-A and SIGMA-B sites in July of all years in the  
560 study period. Each relative frequency represents the fraction of the total contained in each  $10 \text{ W}$   
561  $\text{m}^{-2}$  bin.

## 562 6. Data availability

563 The Level 1.1, 1.2, and 1.3 datasets from this study are archived and available from the Arctic Data  
564 archive System (ADS) in the National Institute of Polar Research (Table 4), where they are stored in  
565 text (CSV) file format. Detailed information on the data content is presented in the file  
566 “data\_format\_site-name\_data-level.csv” associated with each of these dataset files.

567

568 Table 4. Information for the archived datasets from the SIGMA-A and SIGMA-B sites.





<i>SIGMA-A</i>	
Level 1.1	
data name:	Quality-controlled datasets of Automatic Weather Station (AWS) at SIGMA-A site from 2012 to 2020: Level: 1.1
file name:	SIGMA_AWS_SiteA_2012-2020_Lv1_1.csv
citation:	<a href="http://doi.org/10.17592/001.2022041301">http://doi.org/10.17592/001.2022041301</a>
reference:	Nishimura et al. (2023a)
Level 1.2	
data name:	Quality-controlled datasets of Automatic Weather Station (AWS) at SIGMA-A site from 2012 to 2020: Level: 1.2
file name:	SIGMA_AWS_SiteA_2012-2020_Lv1_2.csv
citation:	<a href="http://doi.org/10.17592/001.2022041302">http://doi.org/10.17592/001.2022041302</a>
reference:	Nishimura et al. (2023b)
Level 1.3	
data name:	Quality-controlled datasets of Automatic Weather Station (AWS) at SIGMA-A site from 2012 to 2020: Level: 1.3
file name:	SIGMA_AWS_SiteA_2012-2020_Lv1_3.csv
citation:	<a href="http://doi.org/10.17592/001.2022041303">http://doi.org/10.17592/001.2022041303</a>
reference:	Nishimura et al. (2023c)
<i>SIGMA-B</i>	
Level 1.1	
data name:	Quality-controlled datasets of Automatic Weather Station (AWS) at SIGMA-B site from 2012 to 2020: Level: 1.1
file name:	SIGMA_AWS_SiteB_2012-2020_Lv1_1.csv
citation:	<a href="http://doi.org/10.17592/001.2022041304">http://doi.org/10.17592/001.2022041304</a>
reference:	Nishimura et al. (2023d)
Level 1.2	
data name:	Quality-controlled datasets of Automatic Weather Station (AWS) at SIGMA-B site from 2012 to 2020: Level: 1.2
file name:	SIGMA_AWS_SiteB_2012-2020_Lv1_2.csv
citation:	<a href="http://doi.org/10.17592/001.2022041305">http://doi.org/10.17592/001.2022041305</a>
reference:	Nishimura et al. (2023e)
Level 1.3	
data name:	Quality-controlled datasets of Automatic Weather Station (AWS) at SIGMA-B site from 2012 to 2020: Level: 1.3
file name:	SIGMA_AWS_SiteB_2012-2020_Lv1_3.csv
citation:	<a href="http://doi.org/10.17592/001.2022041306">http://doi.org/10.17592/001.2022041306</a>
reference:	Nishimura et al. (2023f)

569

## 570 7. Summary and conclusion

571 This paper describes the in situ meteorological datasets from the SIGMA-A and SIGMA-B AWS  
572 sites in northwest Greenland and details the QC methods used in preparing the datasets. At this time  
573 when drastic environmental change is proceeding in the Arctic region, sound meteorological data and  
574 QC methods are of ever-growing importance.

575 The QC method offered here consists of two basic steps. The first step, the initial control, masks  
576 observations that are affected by mechanical malfunctions or local phenomena and is a pre-treatment  
577 for the second QC step. This step uses simple statistics to set the range of permissible variation in  
578 northwest Greenland for each observational parameter and flags erroneous records on the basis of that  
579 variation range. The second QC step, the secondary control, masks erroneous observations based on  
580 more stringent variation ranges as determined by the median and SD values of the full observation



581 record. The QC procedures offered here may be valuable for scientists developing their own QC  
582 efforts.

583 We presented examples of time series of air temperature, snow height, PDD, atmospheric pressure,  
584 snow temperature, surface albedos, and longwave radiation based on the resulting hourly  
585 meteorological dataset for 2012–2020 in northwest Greenland. We also extracted information on  
586 climatological cloudiness based on  $LW_{net}$  data derived from these in situ ground observations. Our  
587 primary findings are summarized in the following four points: (1) in the summers of 2015, 2016, 2019,  
588 and 2020, high PDDs and low surface albedos were recorded at both SIGMA-A and SIGMA-B sites.  
589 (2) Dramatic decreases in snow height occurred in 2015 at both AWS sites and in 2016, 2019, and  
590 2020 at the SIGMA-B site. (3) Weather conditions in JJA were relatively variable in northwest  
591 Greenland compared to the other seasons. (4) Clear-sky conditions typified the summers of 2015, 2019,  
592 and 2020.

593 The datasets described here are archived in the open access Arctic Data archive System for all  
594 scientific communities. We anticipate that they will not only aid in understanding and monitoring the  
595 current climate in northwest Greenland but also contribute more broadly to the advancement of polar  
596 climate studies.

597

#### 598 **Author contribution**

599 All authors, excluding M. Nishimura, established the AWS systems and supported their  
600 maintenance. In addition, M. Nishimura developed and carried out the QC procedures and analyzed  
601 the observation data, TA designed and led the study project and provided technical support for the QC  
602 procedures, M. Niwano conducted pre-treatments for the meteorological data record and constructed  
603 a fundamental algorithm of the QC procedures, TY supported the field observations, especially  
604 logistical support, and KF provided advice on interpreting the observational data. All authors  
605 participated in the interpretation of results and gave final approval for publication.

#### 606 **Competing interests**

607 The authors declare that they have no conflict of interest.

#### 608 **Acknowledgments**

609 We recognize all members of the SIGMA project, the GRENE-Arctic Project in Greenland, and  
610 the Arctic Challenge for Sustainability II (ArCS II) project. We also thank all of those who supported  
611 the field observations. In particular, we thank Y. Iizuka (Hokkaido University), Y. Kurosaki (Hokkaido  
612 University), and A. Tsushima (Chiba University) for taking part in the field activities at the SIGMA-  
613 A site and establishing the AWS and Y. Komuro (National Institute of Polar Research) for technical



614 advice. This study was conducted as a part of the “Snow Impurity and Glacial Microbe effects on  
615 abrupt warming in the Arctic (SIGMA)” Project supported by the Japan Society for the Promotion of  
616 Science Grant-in-Aid for Scientific Research numbers JP23221004 and JP16H01772, the Global  
617 Change Observation Mission-Climate (GCOM-C) research project of the Japan Aerospace  
618 Exploration Agency, and ArCS II Program Grant Number JPMXD1420318865. For the use of  
619 NunaGIS (<http://en.nunagis.gl/>) operated by Asiaq, Greenland Survey, in preparing Fig. 1, we  
620 acknowledge the National Snow and Ice Data Center’s QGreenland package (Moon et al., 2021). The  
621 DEM data from Arctic DEMs were provided by the Polar Geospatial Center under NSF-OPP awards  
622 1043681, 1559691, and 1542736.

## 623 References

- 624 Aoki, T., T. Aoki, M. Fukabori, and A. Uchiyama: Numerical simulation of the atmospheric effects  
625 on snow albedo with a multiple scattering radiative transfer model for the atmosphere-snow system,  
626 *J. Meteorol. Soc. Japan*, 77, 595-614, [https://doi.org/10.2151/jmsj1965.77.2\\_595](https://doi.org/10.2151/jmsj1965.77.2_595), 1999.
- 627 Aoki, T., Hachikubo, A., and Hori, M.: Effect of snow physical parameters on shortwave broadband  
628 albedos, *J. Geophys. Res.*, 108, D19, 1–12. <https://doi.org/10.1029/2003jd003506>, 2003.
- 629 Aoki, T., Matoba, S., Uetake, J., Takeuchi, N., and Motoyama, H.: Field activities of the “Snow  
630 Impurity and Glacial Microbe effects on abrupt warming in the Arctic” (SIGMA) Project in  
631 Greenland in 2011-2013. *Bull. Glaciol. Res.*, 32, 3–20. <https://doi.org/10.5331/bgr.32.3>, 2014.
- 632 Armstrong, R. L. and Brun, E. (Eds.): Physical processes within the snow cover and their  
633 parameterization, in *Snow and Climate: Physical Processes, Surface Energy Exchange and*  
634 *Modeling*, Cambridge University Press, Cambridge N.Y., p. 58, 2008.
- 635 Braithwaite, R. J. and Olesen, O. B.: A simple energy-balance model to calculate ice ablation at the  
636 margin of the Greenland ice sheet. *J. Glaciol.*, 36, 222–228.  
637 <https://doi.org/10.1017/S002214300009473>, 1990.
- 638 Brock, B. W. and Arnold, N. S.: A spreadsheet-based (Microsoft Excel) point surface energy balance  
639 model for glacier and snow melt studies. *Earth Surf. Proc. Land.*, 25, 649–658.  
640 [https://doi.org/10.1002/1096-9837\(200006\)25:6<649::AID-ESP97>3.0.CO;2-U](https://doi.org/10.1002/1096-9837(200006)25:6<649::AID-ESP97>3.0.CO;2-U), 2000.
- 641 Estévez, J., Gavilán, P., and Giráldez, J. V.: Guidelines on validation procedures for meteorological  
642 data from automatic weather stations, *J. Hydrol.*, 402, 144–154.  
643 <https://doi.org/10.1016/j.jhydrol.2011.02.031>, 2011.
- 644 Fausto, R. S., van As, D., Mankoff, K. D., Vandecrux, B., Citterio, M., Ahlström, A. P., Andersen, S.  
645 B., Colgan, W., Karlsson, N. B., Kjeldsen, K. K., Korsgaard, N. J., Larsen, S. H., Nielsen, S.,  
646 Pedersen, A., Shields, C. L., Solgaard, A. M., and Box, J. E.: Programme for Monitoring of the  
647 Greenland Ice Sheet (PROMICE) automatic weather station data. *Earth Syst. Sci. Data*, 13, 3819–  
648 3845. <https://doi.org/10.5194/essd-13-3819-2021>, 2021.



- 649 Fettweis, X., Hofer, S., Krebs-Kanzow, U., Amory, C., Aoki, T., Berends, C., Born, A., Box, J.,  
650 Delhasse, A., Fujita, K., Gierz, P., Goelzer, H., Hanna, E., Hashimoto, A., Huybrechts, P., Kapsch,  
651 M.-L., King, M., Kittel, C., Lang, C., L. Langen, P., T. M. Lenaerts, J., E. Liston, G., Lohmann,  
652 G., H. Mernild, S., Mikolajewicz, U., Modali, K., H. Mottram, R., Niwano, M., Noël, B., C. Ryan,  
653 J., Smith, A., Streffing, J., Tedesco, M., J. van de Berg, W., van den Broeke, M., S. W. van de Wal,  
654 R., van Kampenhout, L., Wilton, D., Wouters, B., Ziemen, F., and Zolles, T.: GrSMBMIP:  
655 Intercomparison of the modelled 1980–2012 surface mass balance over the Greenland Ice sheet,  
656 *The Cryosphere*, 1–35. <https://doi.org/10.5194/tc-2019-321>, 2020.
- 657 Fiebrich, C. A., Morgan, Y. R., McCombs, A. G., Hall, P. K., and McPherson, R. A.: Quality assurance  
658 procedures for mesoscale meteorological data. *J. Atmos. Ocean. Tech.*, 27, 1565–1582.  
659 <https://doi.org/10.1175/2010JTECHA1433.1>, 2010.
- 660 Fröhlich, C.: Total solar irradiance observations. *Surv. Geophys.*, 33, 453–473.  
661 <https://doi.org/10.1007/s10712-011-9168-5>, 2012.
- 662 Fujita, K., Matoba, S., Iizuka, Y., Takeuchi, N., Tsushima, A., Kurosaki, Y., and Aoki, T.: Physically  
663 based summer temperature reconstruction from melt layers in ice cores. *Earth Space Sci.*,  
664 8(e2020EA001590), 1–17. <https://doi.org/10.1029/2020EA001590>, 2021.
- 665 Hanna, E., Navarro, F. J., Pattyn, F., Domingues, C. M., Fettweis, X., Ivins, E. R., Nicholls, R. J., Ritz,  
666 C., Smith, B., Tulaczyk, S., Whitehouse, P. L., and Zwally, H. J.: Ice-sheet mass balance and  
667 climate change, *Nature*, 498, 51–59. <https://doi.org/10.1038/nature12238>, 2013.
- 668 Hirose, S., Aoki, T., Niwano, M., Matoba, S., Tanikawa T., Yamaguchi, S., , and Yamasaki, T.:  
669 Surface energy balance observed at the SIGMA-A site on the northwest Greenland ice sheet (in  
670 Japanese with English abstract). *Seppyo*, 83, 143–154, [https://doi.org/10.5331/seppyo.83.2\\_143](https://doi.org/10.5331/seppyo.83.2_143),  
671 2021.
- 672 Hock, R. and Holmgren, B.: A distributed surface energy-balance model for complex topography and  
673 its application to Storglaciären, Sweden, *J. Glaciol.*, 51, 25–36.  
674 <https://doi.org/10.3189/172756505781829566>, 2005.
- 675 IMBIE Team (Shepherd, A. et al.): Mass balance of the Greenland Ice Sheet from 1992 to 2018, *Nature*,  
676 579, 233–239. <https://doi.org/10.1038/s41586-019-1855-2>, 2020.
- 677 IPCC: Summary for Policymakers. In: *Climate Change 2021: The Physical Science Basis*.  
678 Contribution of Working Group I to the Sixth Assessment Report of the Intergovernmental Panel  
679 on Climate Change [Masson-Delmotte, V., P. Zhai, A. Pirani, S. L. Connors, C. P. an, S. Berger,  
680 N. Caud, Y. Chen, L. Goldfarb, M. I. Gomis, M. Huang, K. Leitzell, E. Lonnoy, J.B.R. Matthews,  
681 T. K. Maycock, T. Waterfield, O. Yeleki, R. Yu and B. Zhou (eds.)]. Cambridge University Press.  
682 In Press, 2021.
- 683 Jonsell, U., Hock, R., and Holmgren, B.: Spatial and temporal variations in albedo on Storglaciären,  
684 Sweden, *J. Glaciol.*, 49, 59–68. <https://doi.org/10.3189/172756503781830980>, 2003.



- 685 Kim, H. M. and Kim, B. M.: Relative contributions of atmospheric energy transport and sea ice loss  
686 to the recent warm arctic winter. *J. Clim.*, 30, 7441–7450. [https://doi.org/10.1175/JCLI-D-17-](https://doi.org/10.1175/JCLI-D-17-0157.1)  
687 0157.1, 2017.
- 688 Kurosaki, Y., Matoba, S., Iizuka, Y., Niwano, M., Tanikawa, T., Ando, T., Hori, A., Miyamoto, A.,  
689 Fujita, S., and Aoki, T.: Reconstruction of sea ice concentration in northern Baffin Bay using  
690 deuterium excess in a coastal ice core from the north-western Greenland Ice Sheet. *J. Geophys.*  
691 *Res. Atmos.*, 125. <https://doi.org/10.1029/2019JD031668>, 2020.
- 692 Liang, Y., Bi, H., Huang, H., Lei, R., Liang, X., Cheng, B., and Wang, Y.: Contribution of warm and  
693 moist atmospheric flow to a record minimum July sea ice extent of the Arctic in 2020. *The*  
694 *Cryosphere*, 16, 1107–1123. <https://doi.org/10.5194/tc-16-1107-2022>, 2022.
- 695 Matoba, S., Niwano, M., Tanikawa, T., Iizuka, Y., Yamasaki, T., Kurosaki, Y., Aoki, T., Hashimoto,  
696 A., Hosaka, M., and Sugiyama, S.: Field activities at the SIGMA-A site, north-western Greenland  
697 Ice Sheet, 2017. *Bull. Glaciol. Res.*, 36, 15–22. <https://doi.org/10.5331/BGR.18R01>, 2018.
- 698 Matoba, S., Yamaguchi, S., Tsushima, A., Aoki, T., and Sugiyama, S.: Surface mass balance variations  
699 in a maritime area of the north-western Greenland Ice Sheet (in Japanese with English abstract).  
700 *Low Temperature Science*, 75, 37–44, doi: 10.14943/lowtemsci.75.37, 2017.
- 701 Moon, T., Fisher, M., Harden, L., and Stafford, T.: QGreenland (v1.0.1) [software]. Available from  
702 <https://qgreenland.org>. <https://doi.org/10.5281/zenodo.4558266>, 2021.
- 703 Moradi, I.: Quality control of global solar radiation using sunshine duration hours, *Energy*, 34, 1–6.  
704 <https://doi.org/10.1016/j.energy.2008.09.006>, 2009.
- 705 Morrison, H., De Boer, G., Feingold, G., Harrington, J., Shupe, M. D., and Sulia, K.: Resilience of  
706 persistent Arctic mixed-phase clouds. *Nat. Geosci.*, 5, 11–17. <https://doi.org/10.1038/ngeo1332>,  
707 2012.
- 708 Mougnot, J., Rignot, E., Björk, A. A., van den Broeke, M., Millan, R., Morlighem, M., Noël, B.,  
709 Scheuchl, B., and Wood, M.: Forty-six years of Greenland Ice Sheet mass balance from 1972 to  
710 2018, *P. Natl. Acad. Sci. USA*, 116, 9239–9244. <https://doi.org/10.1073/pnas.1904242116>, 2019.
- 711 Nishimura, M., T. Aoki, M. Niwano, S. Matoba, T. Tanikawa, S. Yamaguchi, T. Yamasaki, A.  
712 Tsushima, K. Fujita, Y. Iizuka, Y. Kurosaki: Quality-controlled datasets of Automatic Weather  
713 Station (AWS) at SIGMA-A site from 2012 to 2020: Level 1.1, 1.00, Arctic Data archive System  
714 (ADS), Japan [dataset], <http://doi.org/10.17592/001.2022041301>, 2023a.
- 715 Nishimura, M., T. Aoki, M. Niwano, S. Matoba, T. Tanikawa, S. Yamaguchi, T. Yamasaki, A.  
716 Tsushima, K. Fujita, Y. Iizuka, Y. Kurosaki: Quality-controlled datasets of Automatic Weather  
717 Station (AWS) at SIGMA-A site from 2012 to 2020: Level 1.2, 1.20, Arctic Data archive System  
718 (ADS), Japan [dataset], <http://doi.org/10.17592/001.2022041302>, 2023b.
- 719 Nishimura, M., T. Aoki, M. Niwano, S. Matoba, T. Tanikawa, S. Yamaguchi, T. Yamasaki, A.  
720 Tsushima, K. Fujita, Y. Iizuka, Y. Kurosaki: Quality-controlled datasets of Automatic Weather



- 721 Station (AWS) at SIGMA-A site from 2012 to 2020: Level 1.3, 1.20, Arctic Data archive System  
722 (ADS), Japan [dataset], <http://doi.org/10.17592/001.2022041303>, 2023c
- 723 Nishimura, M., T. Aoki, M. Niwano, S. Matoba, T. Tanikawa, S. Yamaguchi, T. Yamasaki, K. Fujita:  
724 Quality-controlled datasets of Automatic Weather Station (AWS) at SIGMA-B site from 2012 to  
725 2020: Level 1.1, 1.00, Arctic Data archive System (ADS), Japan [dataset],  
726 <http://doi.org/10.17592/001.2022041304>, 2023d.
- 727 Nishimura, M., T. Aoki, M. Niwano, S. Matoba, T. Tanikawa, S. Yamaguchi, T. Yamasaki, K. Fujita:  
728 Quality-controlled datasets of Automatic Weather Station (AWS) at SIGMA-B site from 2012 to  
729 2020: Level 1.2, 1.10, Arctic Data archive System (ADS), Japan [dataset],  
730 <http://doi.org/10.17592/001.2022041305>, 2023e.
- 731 Nishimura, M., T. Aoki, M. Niwano, S. Matoba, T. Tanikawa, S. Yamaguchi, T. Yamasaki, K. Fujita:  
732 Quality-controlled datasets of Automatic Weather Station (AWS) at SIGMA-B site from 2012 to  
733 2020: Level 1.3, 1.20, Arctic Data archive System (ADS), Japan [dataset],  
734 <http://doi.org/10.17592/001.2022041306>, 2023f.
- 735 Niwano, M., Aoki, T., Matoba, S., Yamaguchi, S., Tanikawa, T., Kuchiki, K., and Motoyama, H.:  
736 Numerical simulation of extreme snowmelt observed at the SIGMA-A site, northwest Greenland,  
737 during summer 2012. *The Cryosphere*, 9, 971–988. <https://doi.org/10.5194/tc-9-971-2015>, 2015.
- 738 Niwano, M., Aoki, T., Hashimoto, A., Matoba, S., Yamaguchi, S., Tanikawa, T., Fujita, K., Tsushima,  
739 A., Iizuka, Y., Shimada, R., and Hori, M.: NHM-SMAP: Spatially and temporally high-resolution  
740 nonhydrostatic atmospheric model coupled with detailed snow process model for Greenland Ice  
741 Sheet. *The Cryosphere*, 12, 635–655. <https://doi.org/10.5194/tc-12-635-2018>, 2018.
- 742 Niwano, M., Box, J. E., Wehrlé, A., Vandecrux, B., Colgan, W. T., and Cappelen, J.: Rainfall on the  
743 Greenland Ice Sheet: Present-day climatology from a high-resolution non-hydrostatic polar  
744 regional climate model. *Geophys. Res. Lett.*, 48(e2021GL092942), 1–11.  
745 <https://doi.org/10.1029/2021GL092942>, 2021.
- 746 Noël, B., van de Berg, W. J., Lhermitte, S., and van den Broeke, M. R.: Rapid ablation zone expansion  
747 amplifies north Greenland mass loss, *Sci. Adv.*, 5, 2–11. <https://doi.org/10.1126/sciadv.aaw0123>,  
748 2019.
- 749 Onuma, Y., Takeuchi, N., Tanaka, S., Nagatsuka, N., Niwano, M., and Aoki, T.: Observations and  
750 modelling of algal growth on a snowpack in north-western Greenland. *The Cryosphere*, 12, 2147–  
751 2158. <https://doi.org/10.5194/tc-12-2147-2018>, 2018.
- 752 Porter, C., Morin, P., Howat, I., Noh, M. J., Bates, B., Peterman, K., Keeseey, S., Schlenk, M., Gardiner,  
753 J., Tomko, K., Willis, M., Kelleher, C., Cloutier, M., Husby, E., Foga, S., Nakamura, H., Platson,  
754 M., Wethington, M. Jr., Williamson, C., Bauer, G., Enos, J., Arnold, G., Kramer, W., Becker, P.,  
755 Doshi, A., D’Souza, C., Cummins, P., Laurier, F., Bojesen, M.: “ArcticDEM”,



- 756 <https://doi.org/10.7910/DVN/OHHUKH>, Harvard Dataverse, V1, [Accessed in January 18, 2022],  
757 2018.
- 758 Rottman, G.: Measurement of total and spectral solar irradiance. *Space Sci. Rev.*, 125, 39–51.  
759 <https://doi.org/10.1007/s11214-006-9045-6>, 2006.
- 760 Ryan, J. C., Smith, L. C., Cooley, S. W., Pearson, B., Wever, N., Keenan, E., and Lenaerts, J. T. M.:  
761 Decreasing surface albedo signifies a growing importance of clouds for Greenland Ice Sheet  
762 meltwater production. *Nat. Comm.*, 13(4205), 1–8. <https://doi.org/10.1038/s41467-022-31434-w>,  
763 2022.
- 764 Shimada, R., Takeuchi, N., and Aoki, T.: Inter-annual and geographical variations in the extent of bare  
765 ice and dark ice on the Greenland ice sheet derived from MODIS satellite images. *Front. Earth*  
766 *Sci.*, 4:43, 1–10. <https://doi.org/10.3389/feart.2016.00043>, 2016.
- 767 Steffen, C. and Box, J. E.: Surface climatology of the Greenland ice sheet: Greenland Climate Network  
768 1995-1999, *J. Geophys. Res.*, 106, D24, 33951–33964, 2001.
- 769 Stramler, K., Del Genio, A. D., and Rossow, W. B.: Synoptically driven Arctic winter states. *J. Clim.*,  
770 24, 1747–1762. <https://doi.org/10.1175/2010JCLI3817.1>, 2011.
- 771 Sugiyama, S., Sakakibara, D., Matsuno, S., Yamaguchi, S., Matoba, S., and Aoki, T.: Initial field  
772 observations on Qaanaaq ice cap, north-western Greenland, *Ann. Glaciol.*, 55, 25–33.  
773 <https://doi.org/10.3189/2014AoG66A102>, 2014.
- 774 Takeuchi, N., Sakaki, R., Uetake, J., Nagatsuka, N., Shimada, R., Niwano, M., and Aoki, T.: Temporal  
775 variations of cryoconite holes and cryoconite coverage on the ablation ice surface of Qaanaaq  
776 Glacier in northwest Greenland. *Ann. Glaciol.*, 59, 21–30. <https://doi.org/10.1017/aog.2018.19>,  
777 2018.
- 778 Tanikawa, T., Hori, M., Aoki, T., Hachikubo, A., Kuchiki, K., Niwano, M., Matoba, S., Yamaguchi, S.,  
779 and Stamnes, K.: In situ measurements of polarization properties of snow surface under the  
780 Brewster geometry in Hokkaido, Japan, and northwest Greenland ice sheet. *J. Geophys. Res.*, 119,  
781 13,946–13,964. <https://doi.org/10.1002/2014JD022325>, 2014.
- 782 Tsutaki, S., Sugiyama, S., Sakakibara, D., Aoki, T., and Niwano, M.: Surface mass balance, ice  
783 velocity and near-surface ice temperature on Qaanaaq Ice Cap, north-western Greenland, from  
784 2012 to 2016, *Ann. Glaciol.*, 58, 181–192. <https://doi.org/10.1017/aog.2017.7>, 2017.
- 785 van As, D., Fausto, R. S., Ahlstrøm, A. P., Andersen, S. B., Andersen, M. L., Citterio, M., Edelvang,  
786 K., Gravesen, P., Machguth, H., Nick, F. M., Nielsen, S., and Anker, W.: Programme for  
787 Monitoring of the Greenland Ice Sheet (PROMICE): First temperature and ablation records, *Geol.*  
788 *Surv. Den. Greenl.*, 23, 73–76. <https://doi.org/10.34194/geusb.v23.4876>, 2011.
- 789 van den Broeke, M., van As, D., Reijmer, C., and van de Wal, R.: Assessing and improving the quality  
790 of unattended radiation observations in Antarctica, *J. Atmos. Ocean. Tech.*, 21, 1417–1431.  
791 [https://doi.org/10.1175/1520-0426\(2004\)021<1417:AAITQO>2.0.CO;2](https://doi.org/10.1175/1520-0426(2004)021<1417:AAITQO>2.0.CO;2), 2004a.



- 792 van den Broeke, M., Reijmer, C., and van de Wal, R.: Surface radiation balance in Antarctica as  
793 measured with automatic weather stations, *J. Geophys. Res.*, 109, D09103, 1–17.  
794 <https://doi.org/10.1029/2003JD004394>, 2004b.
- 795 Wehrli, C.: World Radiation Center (WRC) Publication. Davos-Dorf, Switzerland, 615, pp. 10-17,  
796 1985.
- 797 Wiscombe, W. J., and Warren S. G.: A model for the spectral albedo of snow. I, Pure snow. *J. Atmos.*  
798 *Sci.*, 37, 2712–2733., 1980.
- 799 Yamaguchi, S., Matoba, S., Yamazaki, T., Tsushima, A., Niwano, M., Tanikawa, T., and Aoki, T.:  
800 Glaciological observations in 2012 and 2013 at SIGMA-A site, Northwest Greenland. *Bull.*  
801 *Glaciol. Res.*, 32, 95–105. <https://doi.org/10.5331/bgr.32.95>, 2014.